Computers in Biology and Medicine 150 (2022) 105761

Contents lists available at ScienceDirect

Computers in Biology and Medicine

journal homepage: www.elsevier.com/locate/compbiomed

Additively manufactured lattice structures with controlled transverse isotropy for orthopedic porous implants

Markel Alaña [a,*], Aitziber Lopez-Arancibia [a], Shaaz Ghouse [b], Naiara Rodriguez-Florez [a,c], Sergio Ruiz de Galarreta [a]

[a] Department of Mechanical Engineering and Materials, Universidad de Navarra, TECNUN Escuela de Ingenieros, Paseo Manuel de Lardizabal, 13, 20018 San Sebastian, Spain
[b] Department of Mechanical Engineering, Imperial College London, South Kensington London SW7 2AZ, UK
[c] IKERBASQUE, Basque Foundation for Science, Plaza Euskadi 5, 48009, Bilbao, Spain

ARTICLE INFO

Keywords:
Lattice structures
Transverse isotropy
Orthopedic implants
Additive manufacturing

ABSTRACT

Additively manufactured lattice structures enable the design of tissue scaffolds with tailored mechanical properties, which can be implemented in porous biomaterials. The adaptation of bone to physiological loads results in anisotropic bone tissue properties which are optimized for site-specific loads; therefore, some bone sites are stiffer and stronger along the principal load direction compared to other orientations. In this work, a semi-analytical model was developed for the design of transversely isotropic lattice structures that can mimic the anisotropy characteristics of different types of bone tissue. Several design possibilities were explored, and a particular unit cell, which was best suited for additive manufacturing was further analyzed. The design of the unit cell was parameterized and in-silico analysis was performed via Finite Element Analysis. The structures were manufactured additively in metal and tested under compressive loads in different orientations. Finite element analysis showed good correlation with the semi-analytical model, especially for elastic constants with low relative densities. The anisotropy measured experimentally showed a variable accuracy, highlighting the deviations from designs to additively manufactured parts. Overall, the proposed model enables to exploit the anisotropy of lattice structures to design lighter scaffolds with higher porosity and increased permeability by aligning the scaffold with the principal direction of the load.

1. Introduction

The advances in additive manufacturing (AM) in recent years paved the way for the manufacturing of lattice structures [1]. AM includes many different categories such as direct energy deposition (DED), material extrusion or powder bed fusion (PFB), among others [2]. PBF in general, and selective laser melting (SLM) in particular, offers the possibility to produce complex parts with very small feature sizes, which makes it ideal for the manufacturing of scaffolds for bone tissue engineering [3]. Lattice structures may be formed by stochastic patterns or by predefined unit cells that fill the space to form a part [4]. The mechanical properties of such parts can therefore be tuned by adjusting the topology of the lattice structures forming them [5].

This has brought the attention of several fields, including the biomedical [6,7], since lattice structures may be used as meta-biomaterials for orthopedic implants or bone tissue scaffolds. Bulk metals used for orthopedic implants have an elastic modulus 1 or 2 orders of magnitude higher than host bone [8]. This mismatch of stiffness creates a stress shielding effect, which weakens the bone surrounding the implant, and might lead to implant loosening [8–10]. On the one hand, lattice structures prevent the stress shielding due to their lower stiffness level [11]; and on the other hand, they promote bone ingrowth within the implant due to the interconnected pore network, improving its fixation and stability [12].

Bone tissue exhibits different levels of anisotropy depending on volume fraction and anatomical site [13–16]. Such anisotropy is highly influenced by the mechanoadaptation in bone, which reflects the complex loading environment the bone is subjected to. For example, it has been shown that anisotropy has a profound effect in peri-implant stress and strain in personalized mandibles [17] and maxillas [18], or in the biomechanical behavior of the acetabular cup implant [19]. Thus, matching not only the stiffness levels, but also anisotropy of host bone when designing a lattice structure has the potential to better mimic the mechanical behavior of bone [20]. On the other hand, for bone substitutes in a location where physiological load has a clear principal

* Corresponding author.
E-mail address: malana@tecnun.es (M. Alaña).

https://doi.org/10.1016/j.compbiomed.2022.105761
Received 16 March 2022; Received in revised form 31 May 2022; Accepted 18 June 2022
Available online 3 August 2022

orientation (such as the proximal tibia [21], the spine [22] or the femur [23], where the loading is predominantly compressive and along the anatomical axis), anisotropy can be used to reduce the density of the lattice structure in the orientations other than the principal one, thus enhancing permeability and mass transport of the scaffold, while maintaining the strength and stiffness levels in the principal direction.

Many studies focus on the design of isotropic metamaterials [24–26], and numerical and experimental studies have been performed to determine the mechanical properties of different lattice structures. Nevertheless, most of the literature is focused on uniaxial load in a unique direction (commonly building direction), while this might not necessarily coincide with the main load direction of the implant. Challis et al. [27] and Xu et al. [28] studied the anisotropy of several lattice structures numerically, and developed some macroscopically isotropic structures. Cutolo et al. [29] and Munford et al. [30] tested different lattice structures in several directions to derive their directional stiffness, and Hossain et al. [31] also designed and tested isotropic stochastic structures. Some analytical models that define the permeability [32] and stiffness [33,34] of lattice structures have also been developed in the literature. These models implemented together into optimization algorithms can be a powerful tool to design optimal implants considering both the mechanical performance and the fixation of the implant.

One way to obtain lattice structures with a unique principal direction is to develop transversely isotropic lattice structures, which also corresponds to bone tissue in certain locations [35,36]. In this work a semi-analytical model is developed to design transversely isotropic stretch dominated lattice structures, with prescribed ratios of Young's moduli. This model can be used to design scaffolds that better mimic the patient bone properties to maintain physiological load transfer and to reduce the distortions in stress and strain caused by the implant. The model also enables the design of personalized implants optimized for the anatomical site and patient characteristics. The model was based on previous studies of Hutchinson and Fleck [37], Tancogne-Dejean and Mohr [25], and Messner et al. [24], which were modified to set transverse isotropy as design objective.

2. Materials and methods

2.1. Semi-analytical model

2.1.1. Elastic behavior

In order to describe the mechanical behavior of a periodic lattice it was assumed that the structures are stretch dominated: the bending and torsion of the beams is neglected, and struts are considered to deform axially and rotate freely at the joints. Under this assumption, the stiffness matrix of any strut based lattice structure can be defined as done by Tancogne-Dejean and Mohr [25] and Messner et al. [24], with Eq. (1), where E_s is the Young's modulus of the constituent material, $l^{(i)}$ is the length of each strut, unit vector $\underline{\boldsymbol{n}}^{(i)}$ represents the strut direction, $A^{(i)}$ is the constant cross-section area of the strut, and V_0 defines the volume of the unit cell.

$$\underline{\underline{\underline{\underline{\boldsymbol{C}}}}} = E_s \sum_{i=1}^{N_{struts}} c^{(i)}\, \underline{\boldsymbol{n}}^{(i)} \otimes \underline{\boldsymbol{n}}^{(i)} \otimes \underline{\boldsymbol{n}}^{(i)} \otimes \underline{\boldsymbol{n}}^{(i)}, \quad \text{where } c^{(i)} = \frac{A^{(i)} l^{(i)}}{V_0} \tag{1}$$

This tensor can be represented in the common 6x6 matrix notation, with each component of the matrix defined as C_{ijkl} obtained from Eq. (1), and assuming an orthotropic material model. Fig. 1 defines the orthogonal directions used as subscripts of the stiffness matrix, together with some important directions defined with the Miller indices [100], [110], [101], [111] and [001], and the isotropic 1–2 plane.

$$\boldsymbol{C} = \begin{bmatrix} C_{1111} & C_{1122} & C_{1133} & 0 & 0 & 0 \\ & C_{2222} & C_{2233} & 0 & 0 & 0 \\ & & C_{3333} & 0 & 0 & 0 \\ & & & C_{2323} & 0 & 0 \\ & sym & & & C_{1313} & 0 \\ & & & & & C_{1212} \end{bmatrix} \tag{2}$$

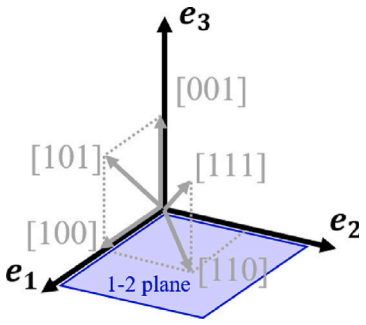

Fig. 1. Coordinate system used to define 1, 2 and 3 orientations in the semi-analytical model, main directions according to the Miller indices ([100], [110], [101], [111] and [001]), and 1–2 isotropic plane.

Eq. (3) defines a relevant property of the stiffness matrix: for a stretch dominated lattice structure that fulfills the stated assumptions it can be stated that $C_{iijj} = C_{ijij}$. Thus, the equivalent homogenized metamaterial can be defined with a maximum of six independent material constants, instead of nine as in any generalized orthotropic material.

$$C_{jjkk} = E_s \sum_{i=1}^{N_{struts}} c^{(i)} (n_j^{(i)})^2 (n_k^{(i)})^2 = C_{jkjk} \tag{3}$$

On the other hand, Tancogne-Dejean and Mohr [25] show that under the stated assumptions, the sum of the stiffness matrix components equals the simple relative density (ρ_{simple}) of the structure multiplied by the Young's modulus of the material, as given in Eq. (4) (note that restrictions in Eq. (3) were included):

$$C_{1111} + C_{2222} + C_{3333} + 2C_{1122} + 2C_{1133} + 2C_{2233} = \rho_{simple} E_s \tag{4}$$

In Eq. (4) the parameter ρ_{simple} is defined as the total sum of relative densities of each individual strut, without considering the overlap at the nodes. A correction fit was applied with the form of an exponential curve to enhance the validity of the model, considering that the fraction of the mass at the nodes is not negligible. This fit relates the theoretical ρ_{simple} obtained from the simple sum of volume fractions, and ρ_{real}, which represents the real relative density of the structures:

$$\rho_{simple} = C_D (\rho_{real})^{n_D} \tag{5}$$

As stated above, the 1–2 plane is considered to be isotropic (see Fig. 1). This condition is enforced assuming that the elastic components in direction 1 are equal to the direction 2 ($C_{1111} = C_{2222}$ and $E_1 = E_2$), and that the elastic components in plane 1–3 are equal to the plane 2–3 ($C_{1133} = C_{2233}$, $G_{13} = G_{23}$ and $\nu_{13} = \nu_{23}$). Furthermore, the transverse isotropy condition must hold Eq. (6), which can be simplified by using Eq. (3):

$$C_{1111} - C_{1122} = 2C_{1212} \rightarrow C_{1111} = 3C_{1122} \tag{6}$$

With the imposed restrictions for transverse isotropy, the stiffness matrix can be defined as a function of the effective elastic constants of the structure (E_1, E_3, ν_{12}, ν_{13} and G_{13}) as done in Eq. (7). Note that for isotropy in 1–2 plane $G_{12} = E_1/2(1+\nu_{12})$ must be fulfilled. Thus, Eq. (7) relates the elastic constants with the effective stiffness matrix of the structure. Furthermore, Eq. (6) can also be rewritten in terms of elastic constants, as done in Eq. (8).

$$\boldsymbol{C} = \boldsymbol{S}^{-1} = \begin{bmatrix} \frac{1}{E_1} & \frac{-\nu_{12}}{E_1} & \frac{-\nu_{13}}{E_1} & 0 & 0 & 0 \\ & \frac{1}{E_1} & \frac{-\nu_{13}}{E_1} & 0 & 0 & 0 \\ & & \frac{1}{E_3} & 0 & 0 & 0 \\ & & & \frac{1}{G_{13}} & 0 & 0 \\ & sym & & & \frac{1}{G_{13}} & 0 \\ & & & & & \frac{2(1+\nu_{12})}{E_1} \end{bmatrix}^{-1} \tag{7}$$

Table 1
Values of ν_{12} obtained by linear least square approximation as a function of E_3/E_1.

E_3/E_1 [–]	1.0	1.25	1.5	1.75	2.0	2.25	2.5	2.75	3.0
ν_{12} [–]	0.2500	0.2518	0.2560	0.2612	0.2667	0.2722	0.2775	0.2824	0.2870

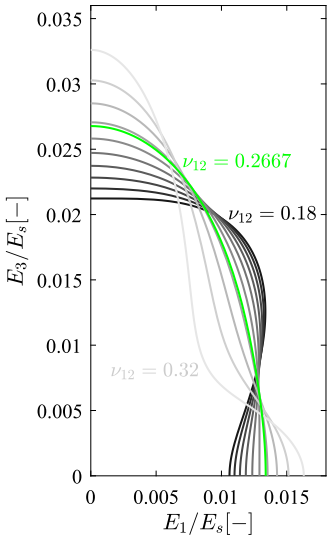

Fig. 2. Directional stiffness for constant ρ_{real} and $E_3/E_1 = 2$, and varying ν_{12}.

$$4\frac{E_3}{E_1}\nu_{13}^2 + 3\nu_{12} - 1 = 0 \tag{8}$$

Eqs. (4) and (5) and the stiffness matrix symmetries for transverse isotropy can be introduced in Eq. (7) to obtain the stiffness matrix of any stretch dominated transversely isotropic lattice as defined in Eq. (9). Thus, the stiffness of the structures is defined as a function of the Young's modulus of the constituent material (E_s), the ratio between stiffness in principal direction 3 and the transverse plane (E_3/E_1), the Poisson's ratios ν_{12} and ν_{13} (note that Eq. (8) should also be fulfilled), the relative density of the structure (ρ_{real}), and the parameters C_D and n_D.

$$\boldsymbol{C} = \frac{3C_D(\rho_{real})^{n_D}E_s}{4[2+\frac{E_3}{E_1}(1-\nu_{12}+4\nu_{13})]} \times \begin{bmatrix} 1 & 1/3 & \frac{4}{3}\frac{E_3}{E_1}\nu_{13} & 0 & 0 & 0 \\ & 1 & \frac{4}{3}\frac{E_3}{E_1}\nu_{13} & 0 & 0 & 0 \\ & & \frac{4}{3}\frac{E_3}{E_1}(1-\nu_{12}) & 0 & 0 & 0 \\ & & & \frac{4}{3}\frac{E_3}{E_1}\nu_{13} & 0 & 0 \\ & sym & & & \frac{4}{3}\frac{E_3}{E_1}\nu_{13} & 0 \\ & & & & & 1/3 \end{bmatrix} \tag{9}$$

For a given ρ_{real} and E_3/E_1 ratio, there are infinitely many possible configurations that fulfill the transverse isotropy condition, depending on ν_{12} or ν_{13}. Fig. 2 depicts the directional stiffness for different values of ν_{12}, with constant ρ_{real} and E_3/E_1.

The parameter ν_{12} was chosen so that the change of stiffness is as smooth as possible. Thus, the directional stiffness fits an ellipse in the 1–3 plane with axes E_1 and E_3, and an equivalent ellipsoid in 3D space (green curve in Fig. 2). This was done by using the MATLAB Curve Fitting Toolbox, and the obtained results of ν_{12} for different E_3/E_1 ratios are shown in Table 1. Note that $E_3/E_1 = 1$ is a particular case of the model that corresponds to elastically isotropic behavior. The E_3/E_1 ratios were chosen to be of interest for bone substitutes in the proximal tibia, spine and femur [20,30].

2.1.2. Unit cell design

Eq. (9) defines the stiffness matrix of any transversely isotropic stretch dominated structure, while Eq. (1) relates the stiffness matrix with the geometric variables of the lattice structure: the orientation, length, and cross-section area of the struts ($\underline{\boldsymbol{n}}^{(i)}$, $l^{(i)}$ and $A^{(i)}$, respectively). This can be used to design a unit cell that actually fits in the imposed stiffness matrix. Before obtaining such geometric parameters it is necessary to define a strut configuration that might comply with the imposed restrictions. Furthermore, the parameters C_D and n_D are morphology dependent, and strut configuration must be known to define them. Fig. 3 depicts the process of the design of a transversely isotropic unit cell, with E_3/E_1, ρ_{simple}, Es and strut configuration as input values, and the diameters and aspect ratio (K) as output parameters. The parameter ρ_{real} is an input value once the C_D and n_D coefficients are obtained, but it also can be considered an output value needed to obtain such coefficients for a set of given ρ_{simple} values.

Different combinations of well-known unit cells were used to build the structures, namely SC, BCC and FCC. Fig. 4 depicts those unit cells, while each color represents a different diameter value. Note that for SC and FCC two different diameters were assigned in each unit cell, whereas BCC has a unique diameter. These diameters are the design variables that allow the combined unit cells to comply with stiffness matrix in Eq. (9). Furthermore, another design parameter was included among the variables to widen the range of possible designs: the aspect ratio between the height and width of the unit cell, represented as K.

The arrangement of the diameter variables implicitly imposes $C_{1111} = C_{2222}$ and $C_{1133} = C_{2233}$. In addition, it can be proved that any unit cell needs at least 4 design variables to comply with a transversely isotropic stiffness matrix as defined in Eq. (9). Thus, the unit cells in Fig. 4 must be combined so that they offer 4 different design parameters. These are some of the possibilities:

- SC2BCC: SC with 2 diameters, and BCC with a unique diameter. Thus, a variable height to width ratio K is added to comply with transverse isotropy (Fig. 5(a)).
- SC2FCC2: A combination of SC and FCC unit cells, with two different diameters each (Fig. 5(b)).
- VFCCBCC: Combination of vertical struts (V), FCC struts out of the isotropic plane and BCC struts, also considering variable height to width ratio K (Fig. 5(c)).

It should be noted that one of the challenges of SLM technology is to fabricate horizontal struts (parallel to the building plate) that guarantee the required quality from a structural point of view. In order to overcome this limitation, the unit cell choice for this study was the VFCCBCC (Fig. 5(c)) which offers the possibility to orient the mass of the unit cell so that the orientation of the BCC and FCC struts compensate the lack of horizontal struts with their lower angle with respect to the building plane. Therefore, the VFCCBCC unit cell was chosen for the rest of the numerical validation and experimental analysis.

2.1.3. Elastic constants

For a given ρ_{real}, E_3/E_1, and ν_{12} (obtained as in Table 1, and provided that Eq. (8) holds), it is possible to analytically obtain the transversely isotropic stiffness matrix of any of the proposed unit cells, as well as the design parameters (diameters and K) that result in such elastic response.

The elastic behavior of the proposed model depends on the unit cell of the structures due to the adjustment between simple relative density

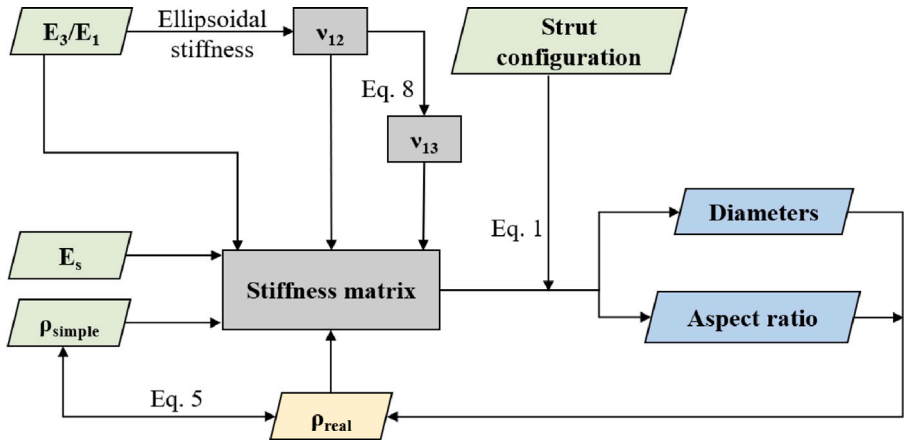

Fig. 3. Design process of unit cells under the constraints of transversal isotropy.

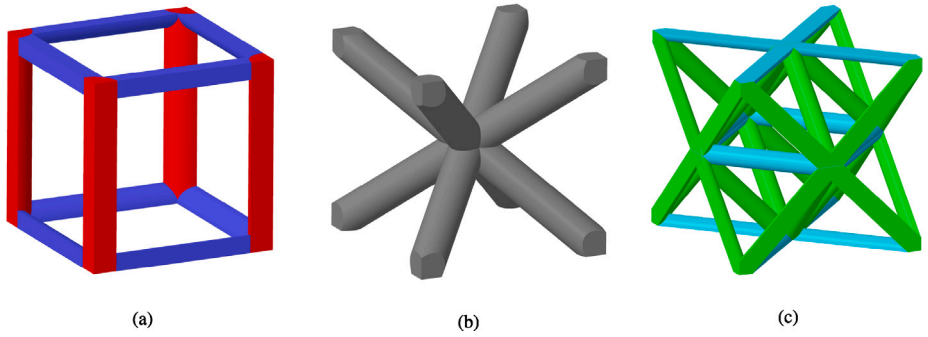

Fig. 4. Basic unit cells to combine in order to form transversely isotropic lattices: (a) SC, (b) BCC, and (c) FCC.

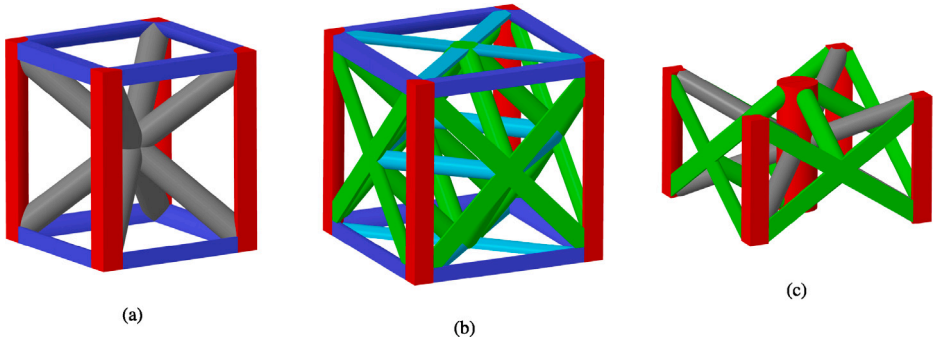

Fig. 5. Unit cells of (a) SC2BCC, (b) SC2FCC2, and (c) VFCCBCC, with each strut color representing a different cross-section variable.

(sum of volume of each strut) and actual relative density (Eq. (5)). In order to derive C_D and n_D parameters, different VFCCBCC configurations were designed with different relative densities and E_3/E_1 ratios (it was observed that the latter could be neglected for the relative density adjustment).

Thus, the normalized elastic constants for the VFCCBCC lattice structure (also valid for the other unit cells) are obtained as a function of ρ_{real}, E_3/E_1, and ν_{12} as described below:

$$\frac{E_1}{E_s} = \frac{E_2}{E_s} = C_D(\rho_{real})^{n_D} \frac{(1+\nu_{12})}{4+\frac{E_3}{E_1}[2(1-\nu_{12})+8\nu_{13}]} \tag{10}$$

$$\frac{E_3}{E_s} = C_D(\rho_{real})^{n_D} \frac{\frac{E_3}{E_1}(1+\nu_{12})}{4+\frac{E_3}{E_1}[2(1-\nu_{12})+8\nu_{13}]} \tag{11}$$

$$\frac{G_{13}}{E_s} = \frac{G_{23}}{E_s} = C_D(\rho_{real})^{n_D} \frac{\frac{E_3}{E_1}\nu_{13}}{2+\frac{E_3}{E_1}[(1-\nu_{12})+4\nu_{13}]} \tag{12}$$

The model is semi-analytical because the parameters C_D, n_D and ν_{12} are obtained by least square approximations.

2.1.4. Yield strength

The strength of an implant has to be sufficient to withstand the physiological loads of each bone site, and a predictive tool for the strength of the scaffolds is necessary for their application in orthopedic implants. Thus, a semi-analytical model was developed to define the effective yield strength of the VFCCBCC structure. The stress at each strut under an effective macroscopic stress was calculated using Eq. (13). In this equation the scalar values with superscript (i) correspond to parameters of each strut: $\sigma^{(i)}$ and $\varepsilon^{(i)}$ are the stress and axial strain of the strut (i), respectively, and $\underline{\boldsymbol{n}}^{(i)}$ defines the unit vector of the strut orientation. E_s is the Young's modulus of the constituent material, $\underline{\underline{\underline{\underline{\boldsymbol{S}}}}}$ defines the macroscopic compliance matrix of the structure and $\underline{\underline{\boldsymbol{\sigma}_{eff}}}$ corresponds to the macroscopic effective stress applied to the structure.

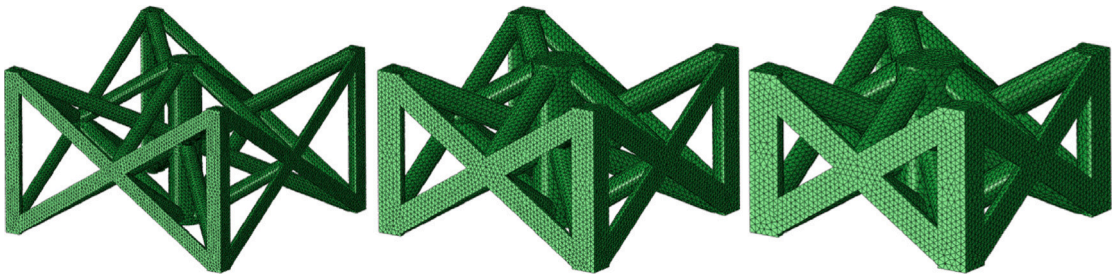

Fig. 6. Numerical models of the VFCCBCC unit cell with $E_3/E_1 = 2$ and varying relative densities of 0.09, 0.2 and 0.3.

Table 2
Material properties for FE model.

Young's modulus [GPa]	Poisson's ratio [–]	Yield strength [MPa]	Tangent modulus [MPa]
190	0.3	453	260

Table 3
Diameters of manufactured structures for both relative densities.

		Diameters [mm]		
Structure	Relative density [%]	Vertical (angle)	FCC (angle)	BCC (angle)
A	12.5	0.47 (90.0)	0.22 (33.0)	0.23 (24.7)
B	25.0	0.70 (90.0)	0.33 (33.0)	0.35 (24.7)

$$\sigma^{(i)} = E_s \varepsilon^{(i)} = E_s \left[\underline{\underline{\underline{\boldsymbol{S}}}} : (\underline{\boldsymbol{n}}^{(i)} \otimes \underline{\boldsymbol{n}}^{(i)}) \right] : \underline{\underline{\boldsymbol{\sigma}_{\boldsymbol{eff}}}} \tag{13}$$

Thus, each strut of the unit cell will have a different stress level, and it will be proportional to the macroscopic effective stress ($\underline{\underline{\boldsymbol{\sigma}_{\boldsymbol{eff}}}}$). The effective yield strength of the structure is calculated as the macroscopic stress that brings at least one strut to the yield strength of the constituent material ($\sigma_{y,s}$), that is $\sigma^{(i)}_{max} = \sigma_{y,s}$. As occurs with stiffness, the effective yield strength varies depending on the orientation of the load. To obtain the directional effective yield strength of the structures, denoted as $\sigma_{eff,y}$, a uniaxial $\underline{\underline{\boldsymbol{\sigma}_{\boldsymbol{eff}}}}$ was applied in various orientations covering all the 3D space, and the magnitude $\sigma_{eff,y}$ was calculated to induce $\sigma_{y,s}$ stress level in the struts.

2.2. Numerical validation

The accuracy of the semi-analytical model and the effect of the relative density on the unit cell was studied with several numerical models built in Abaqus 2020 (Dassault Systems). 9 different unit cells were modeled for each E_3/E_1 ratio with relative densities varying from 1% to 30%, and E_3/E_1 ratios of 1.5, 2, and 3. The relative density of the structures was defined to ensure a high porosity range of the implants needed in scaffold design [38,39]. Fig. 6 depicts some of the analyzed structures with different relative densities. The models where meshed with second order tetrahedral elements and after conducting a mesh sensitivity analysis, the diameter/element size ratio was set to 5 for all the structures.

The material properties of 316L stainless steel were modeled as a bilinear material model, with values given in Table 2 [40].

Periodic Boundary Conditions (PBC) were applied and the code of Omairey [41] was used to get the elastic constants of the VFCCBCC unit cell. Apart from the elastic and shear moduli, the accuracy of the semi-analytical model was also assessed by the E_3/E_1 ratio, as well as the Zener ratio in the 1–2 plane, which gives the measure of elastic isotropy:

$$Z_{12} = \frac{2C_{1212}}{C_{1111} - C_{1122}} \tag{14}$$

On the other hand, uniaxial stress was applied in directions [001], [110], [101], [111], [100] in the VFCCBCC unit cell with different relative densities, and under PBC to numerically calculate the yield strength of the structure.

The criteria to numerically determine the yield strength of the structure had to be adapted from the one used for the analytical model, where the struts were treated as axially loaded beams with a constant stress through the strut. Instead, the criteria to numerically determine the yield stress of the structure was to find the macroscopic stress value where the plastic dissipation energy exceeded 10% of the total energy of the structure, similarly to [25]. The results were compared to the semi-analytically obtained yield strength values.

2.3. Manufacturing

VFCCBCC structures were produced with $E_3/E_1 = 2$ and two different relative densities, 12.5% and 25%, to be tested in three different orientations, namely [100], [110] and [001]. To test 3 samples per density and load orientation, a total of 18 parts were manufactured. Unit cell size was 3 mm, and the manufacturing orientation was the same in all cases to maintain the orientation of every strut with respect to the build plate and prevent unequal imperfection distributions between batches.

All specimens were manufactured on an AM250 metal powder bed fusion machine (Renishaw Plc.) under an inert argon atmosphere from Stainless Steel 316L directly onto a mild steel substrate. The parts were removed from the plate by electro discharge machining. Build files for the specimens were generated from an in-house piece of software, described previously in [42]. The software allows lattices to be defined in a beam format (start and end x,y,z positions) with a desired diameter. Based on the strut angle and desired diameter, laser parameters are assigned accordingly. Laser parameters were assigned to produce the struts of diameter described in Table 3.

The relative density of the produced specimens was measured by weighing the structures and dividing by the theoretical weight of a solid part with the external volume of the structures. On the other hand, to measure strut density Archimedes method was used as done in other studies [43]. This method consists in measuring the weight difference of the part when submerged into ethanol compared to a dry environment (in air) to determine the proportion of internal pores. Eq. (15) defines the strut density (ρ_{strut}) as a function of the weight of the structure in air (w_{air}), the density of ethanol ($\rho_{ethanol}$), the density of 316L stainless steel (ρ_{316L}) and the weight of the structure in ethanol ($w_{ethanol}$).

$$\rho_{strut} = \frac{w_{air}\, \rho_{ethanol}}{\rho_{316L}\, (w_{air} - w_{ethanol})} \tag{15}$$

2.4. Mechanical testing

Compression tests were carried out as per ISO 13314:2011 [44] in an Instron 3360 with a load cell of 30kN except for the structure B in [001] orientation, which was tested in a Instron 5982 with a load cell

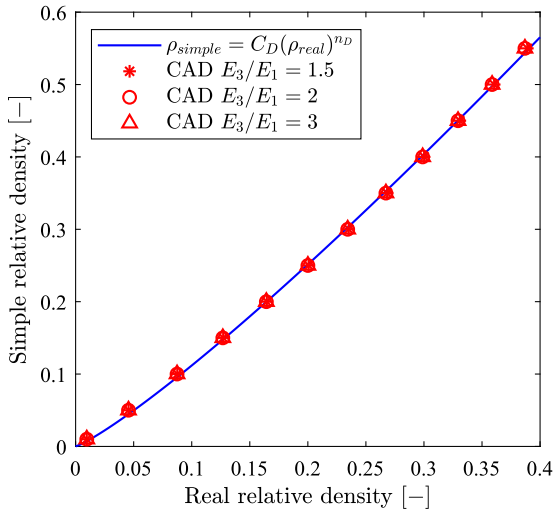

Fig. 7. Designed VFCCBCC structures with different relative densities and E_3/E_1 values, and adjusted curve.

of 100kN due to its higher strength. The tests were performed in three different orientations for each relative density: [001], [100] and [110]. For each relative density and orientation 3 specimens were tested. The strain was calculated after measuring the compliance of the machines. For each specimen quasi-elastic gradient and 0.2% offset stress (yield strength) was calculated.

3. Results

3.1. Semi-analytical model

Fig. 7 depicts the simple relative density (ρ_{simple}) of the VFCCBCC structure as a function of its real relative density (ρ_{real}). The ρ_{real} values were obtained from CAD measurements of models with different E_3/E_1 ratios. The C_D and n_D values derived by least square approximation ($R^2 = 0.999$) are 1.65 and 1.169, respectively. The values for the SC2BCC and SC2FCC2 are displayed in Table S1 (supplementary material).

Fig. 8 shows the yield surface of VFCCBCC unit cells for uniaxial loads in any orientation. The surfaces for $E_3/E_1 = 1.5$, $E_3/E_1 = 2$, and $E_3/E_1 = 3$ are depicted, which are in the bone range (spine trabecular [22], proximal tibia [21] or femur cortical bone [23]). Effective yield strength ($\sigma_{eff,y}$) is obtained from Eq. (13), and normalized with the density variable $C_D(\rho_{real})^{n_D}$ and the yield strength of the constituent material ($\sigma_{y,s}$). It can be observed that for any E_3/E_1 ratio, the structure is weaker in the directions that coincide with strut orientations, because the load is primarily carried by a single strut. On the contrary, in other orientations the load is more effectively distributed among struts. The effective strength in the transverse plane reduces with the increase of E_3/E_1 ratio, while the strength in [001] increases.

Fig. 9 depicts the values of normalized yield strength of VFCCBCC for different E_3/E_1 ratios, under [001] and [110] orientations, since the latter is the weakest orientation in the transverse plane. Thus, the effective yield strength of the structure can be directly calculated for any relative density by multiplying the normalized strength value with the yield strength of the constituent material. The strength ratio between the [001] and [110] plane is always lower than the E_3/E_1 ratio, with values of 1.21, 1.60 and 2.41 for E_3/E_1 of 1.5, 2, and 3, respectively.

3.2. Finite element validation

3.2.1. Elastic behavior

The results of the numerical simulations of VFCCBCC unit cells with $E_3/E_1 = 1.5$, $E_3/E_1 = 2$, $E_3/E_1 = 3$ are depicted in Fig. 10, showing the elastic constants E_1, E_3, G_{12}, G_{13}, ν_{12}, and ν_{13}, and comparing the obtained values with the semi-analytical model obtained from Eqs. (8), (10)–(12). In general, a very good agreement between the FE analysis and the semi-analytical model can be observed, especially for low relative densities, and the error increases with the relative density.

In the case of effective Young's modulus, E_3 is more accurate than E_1 for any E_3/E_1 ratio. The R^2 coefficients for E_1 lay between 0.885 and 0.941, whereas for E_3 the R^2 values are higher than 0.989 for any E_3/E_1 ratio. This occurs because the assumption of pure axial stress is better fulfilled in [001] orientation due to the vertical struts of the VFCCBCC unit cell, while for [100] this assumption is not as valid for moderate relative densities. As a result, the maximum relative error arises for the highest studied relative density of 0.3. In this case, the maximum error of E_1 is 22.8% for $E_3/E_1 = 3$, and in the case of E_3 the maximum relative error is 7.8% for $E_3/E_1 = 1.5$.

The accuracy of the shear moduli is lower than for Young's moduli. For G_{12} the R^2 value is between 0.878 ($E_3/E_1 = 3$) and 0.938 ($E_3/E_1 = 1.5$), while G_{13} has R^2 coefficients between 0.930 ($E_3/E_1 = 3$) and 0.954 ($E_3/E_1 = 1.5$). For $\rho_{real} = 0.3$, the maximum relative error for G_{12} is 23.8% and for G_{13} equals 17.7% ($E_3/E_1 = 3$ in both cases). For Poisson's ratios, the maximum error values of ν_{12} are 7.9%, 6.7% and 6.1% for $E_3/E_1 = 1.5$, $E_3/E_1 = 2$ and $E_3/E_1 = 3$, respectively, and 7.2%, 10.7% and 17.8% for ν_{13}. Fig. 10(d) depicts the 3D stiffness of the FE model with a $\rho_{real} = 0.2$ and $E_3/E_1 = 2$. The directional stiffness has the expected ellipsoidal shape, the change in stiffness is smooth and the variability in the 1–2 plane is very small (below 0.1%).

As depicted in Fig. 11(a), the accuracy of the E_3/E_1 ratio is very high for low relative densities, but decreases with increased relative density for any of the studied cases. This is a consequence of the bending that increases the stiffness more in direction [100] compared to [001], as also observed in Fig. 10(a). Furthermore, as prescribed E_3/E_1 increases, the error of the semi-analytical model also increases. For $\rho_{real} = 0.3$, the relative errors of E_3/E_1 are 10.7%, 20% and 33.1% for $E_3/E_1 = 1.5$, $E_3/E_1 = 2$, and $E_3/E_1 = 3$ respectively. On the other hand, the Zener ratio in the 1–2 plane, which measures the elastic isotropy in the plane, and defined in Eq. (14), is depicted in Fig. 11(b) for the three E_3/E_1 ratios, showing that the transverse isotropy is maintained with a relative error below 2.8% for any studied relative density and E_3/E_1 ratio. This suggests that the stiffness added by the bending of struts acts uniformly in the 1–2 plane.

Fig. 12 depicts the Von Mises stress of the VFCCBCC unit cell under pure shear load in the 1–2 plane for two relative densities. The stress of the loaded struts is closer to the assumption of uniaxial uniform stress for thin struts, while in thick struts the bending loads induce non-uniform stresses along the struts. Furthermore, the strut joints have more relevance for higher relative densities, and triaxial stress states arising there affect a larger part of the structure. This explains the gradual loss of accuracy as the relative density increases.

The relative importance of the bending load also depends on the load type and orientation: the loads or deformations aligned with struts result in lower bending loads, which explains the variability of the accuracy for different elastic constants and yield strengths for the same relative density.

3.2.2. Yield strength

The accuracy of the semi-analytical model (Eq. (13)) to predict the yield strength of the VFCCBCC unit cell varies depending on the load orientation, the E_3/E_1 ratio and the relative density. Fig. 13 shows the yield strength for 5 different orientations, defined as in Fig. 1, and for $E_3/E_1 = 1.5$, $E_3/E_1 = 2$, and $E_3/E_1 = 3$. The semi-analytical yield model has the highest accuracy for [001] and [110] orientations, with

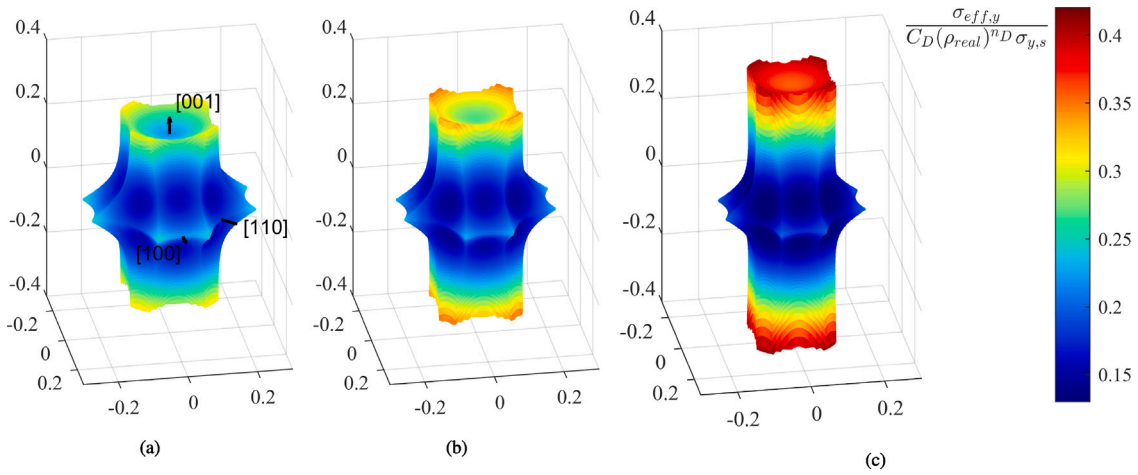

Fig. 8. Semi-analytical yield surface of VFCCBCC in 3D space obtained from Eq. (13) with (a) $E_3/E_1 = 1.5$, (b) $E_3/E_1 = 2$, and (c) $E_3/E_1 = 3$.

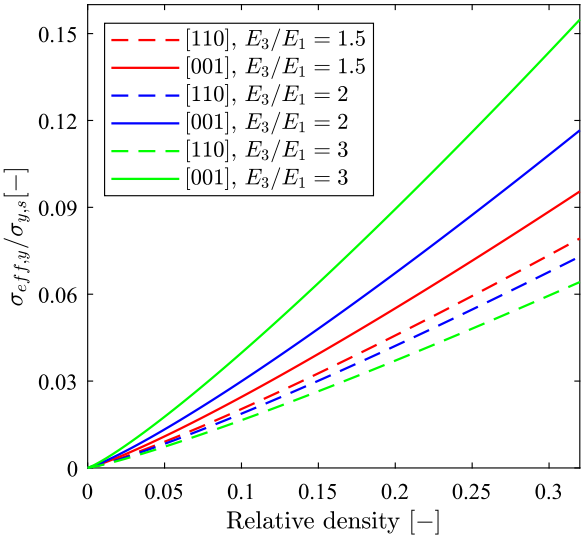

Fig. 9. Yield strength of VFCCBCC for [110] (weakest orientation in transverse plane) and [001] orientations, for different E_3/E_1 ratios.

R^2 values above 0.993 and 0.997, respectively, regardless E_3/E_1 ratios. In orientations [101] and [111] the semi-analytical model slightly underestimates the strength of the structures, but the R^2 coefficients indicate high correlation with minimum values of 0.969 for [101] and 0.955 for [111] for any E_3/E_1 stiffness ratio. On the other hand, the semi-analytical model overestimates the strength in [100] orientation, and the R^2 coefficient increases with E_3/E_1 ratio, with $R^2 = 0.888$ for $E_3/E_1 = 1.5$ and $R^2 = 0.919$ for $E_3/E_1 = 3$.

3.3. Mechanical testing

3.3.1. Morphology of specimens

Specimens of two prescribed relative densities were produced, 12.5% and 25%, and the resulting relative density and strut density properties are given in Table 4. The average differences between the designed and manufactured relative densities were of 2.2% in batch A and 7.3% in batch B. Even if the manufacturing parameters were the same within each batch, a significant variability (relative variability above 10% with respect to the designed value) of the produced relative densities can be observed in batch B. The strut density is above 98% in all cases, indicating some prevalence of internal pores.

Table 4
Relative density and strut density values for produced specimens.

Specimen	Relative density [%]	Strut density [%]
A-[001]	9.77 ± 0.46	98.67 ± 0.58
A-[100]	10.27 ± 0.40	98.45 ± 0.22
A-[110]	9.28 ± 0.40	98.63 ± 0.61
B-[001]	19.44 ± 0.06	99.15 ± 0.17
B-[100]	16.47 ± 0.27	98.88 ± 0.12
B-[110]	17.30 ± 0.69	98.98 ± 0.02

Fig. 14 depicts the actual morphology of the struts, indicating clear deviations from the designed CAD geometry. An important waviness can be observed, especially in the struts with lower angles with respect to the build plate. Moreover, in the thinnest struts the staircase effect that arises from the layer by layer manufacturing process is clearly visible, and this effect is enhanced by the fact that the struts were produced point by point.

3.3.2. Quasi-static compression

The curves obtained from quasi-static compression tests are given in Fig. 15. Figs. 15(a) and 15(b) correspond to the batch A, and Figs. 15(c) and 15(d) depict the compression curves of batch B. The shaded areas in Figs. 15(a) and 15(c) represent the 95% confidence interval, and Figs. 15(b) and 15(d) depict a close-up of the compression curves up to a strain of 0.06, in order to give a better insight into the elastic response of the structures. The stress–strain curves present a expected shape for ductile metals, with a linear region, followed by the yielding of the structures and an energy absorption process up to densification of the structures. The variability within each sample is much higher in the batch A as shown in Fig. 15(a). Furthermore, its lower relative density results in a compression process dominated by buckling with more peaks and valleys.

The obtained mechanical properties are listed in Table 5. For both relative densities the quasi-elastic gradient in direction [001] clearly exceeds the gradient in directions [100] and [110], as would be expected from the design of the structures.

Fig. 16 depicts the anisotropy characteristics of the semi-analytical and numerical models, compared to the experimental values in structures A and B. The E_{110}/E_1 and E_3/E_1 ratios are lower than the analytical values for both manufactured structures, nonetheless, the structure B is in good agreement with the prescribed values (relative error of 3% for E_3/E_1 and 10% for E_{110}/E_1). While the accuracy of the numerical model decreases with higher relative densities (see E_3/E_1 ratios in FEM), this also enables a reduced imperfection level of the manufactured structures, thus reducing the error of the anisotropy with respect to the semi-analytical model (experimental E_3/E_1 and E_{110}/E_1 ratios).

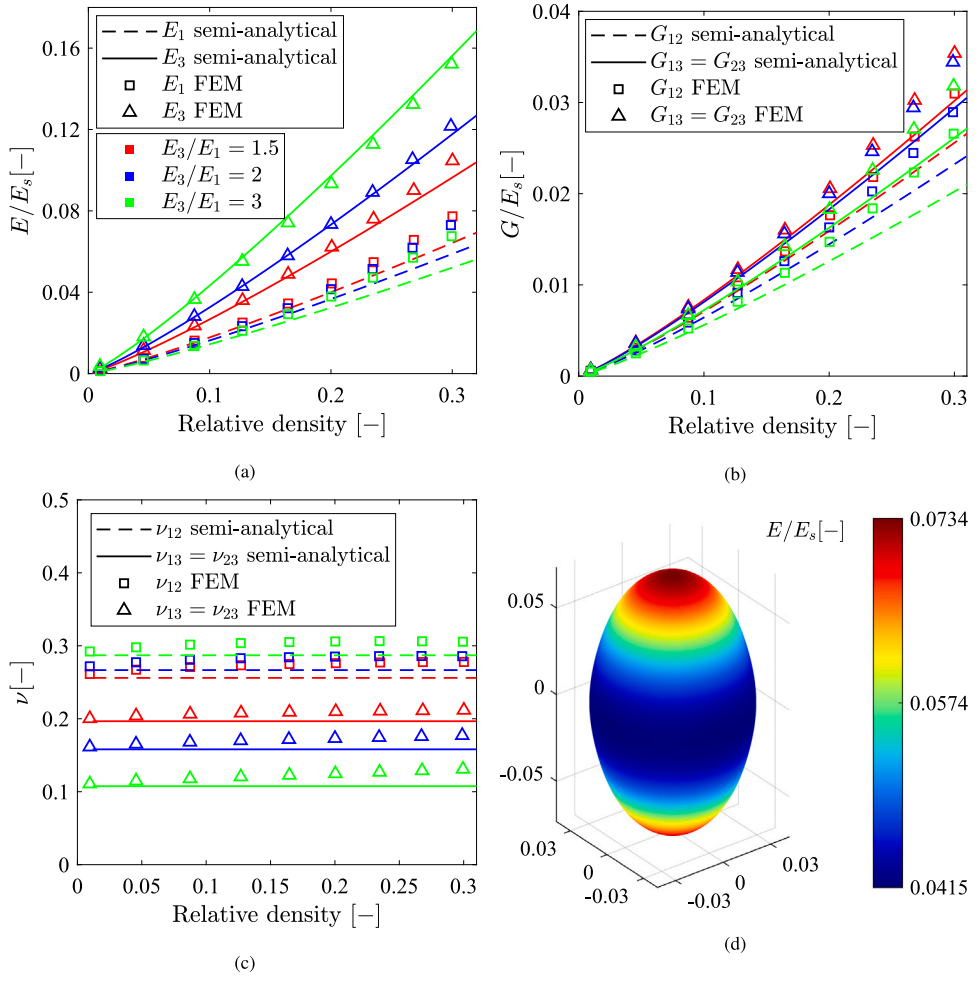

Fig. 10. Semi-analytical and FEM comparison of the elastic behavior of VFCCBCC unit cell for $E_3/E_1 = 1.5$, $E_3/E_1 = 2$ and $E_3/E_1 = 3$: (a) Young's moduli, (b) shear moduli, (c) Poisson's ratios. (d) is the directional homogenized stiffness for $E_3/E_1 = 2$.

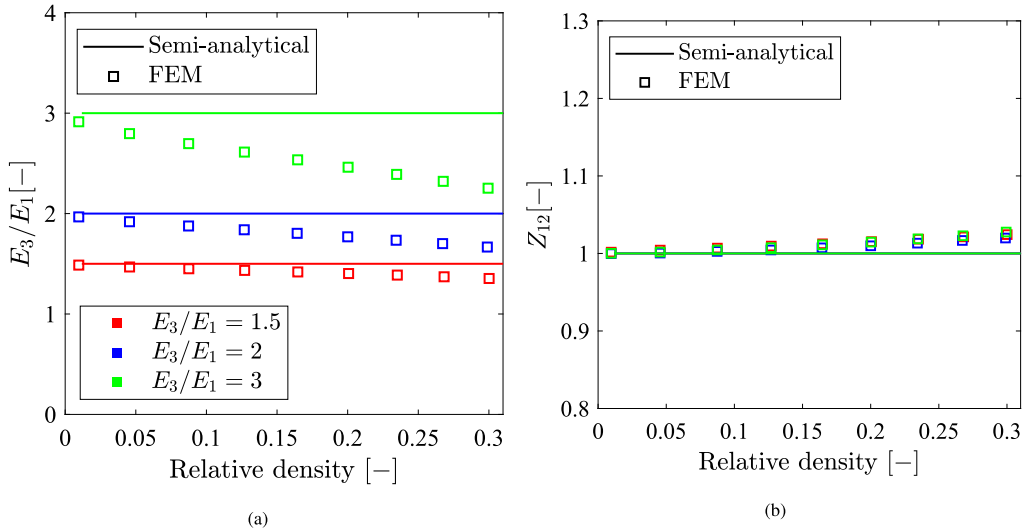

Fig. 11. Semi-analytical and FEM comparison of the elastic behavior of VFCCBCC unit cell for $E_3/E_1 = 1.5$, $E_3/E_1 = 2$ and $E_3/E_1 = 3$: (a) E_3/E_1 ratio, and (b) Zener ratio.

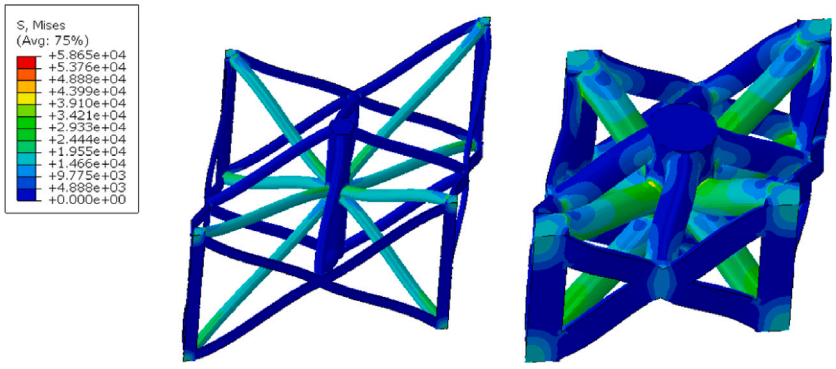

Fig. 12. Von Mises stress of VFCCBCC unit cells with different relative densities under shear load in 1–2 plane.

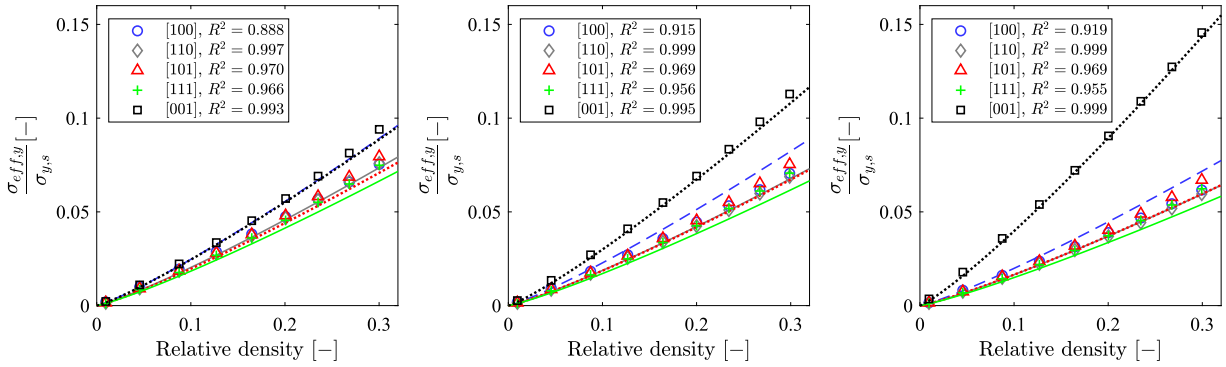

(a) (b) (c)

Fig. 13. Effective yield strength of VFCCBCC unit cell in various orientations, normalized with constituent material yield strength, and for different E_3/E_1 ratios: (a) $E_3/E_1 = 1.5$ (b) $E_3/E_1 = 2$, (c) $E_3/E_1 = 3$.

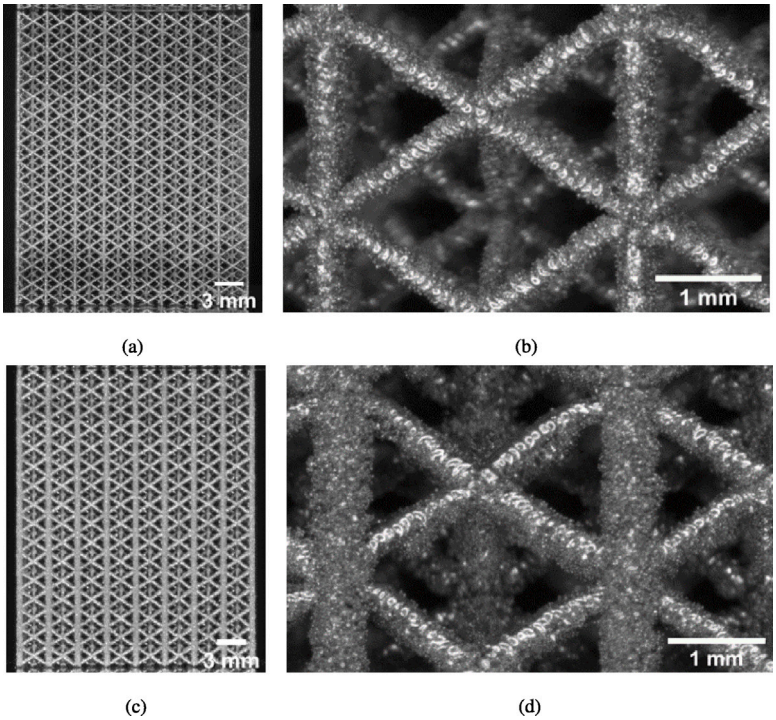

Fig. 14. Manufactured specimens of VFCCBCC structures for loading in [001] corresponding to batch A (a) and (b), and batch B (c) and (d).

Table 5
Results of quasi-static compression tests for batches A and B in directions [001], [100] and [110].

	A			B		
	[001]	[100]	[110]	[001]	[100]	[110]
Quasi-elastic gradient [GPa]	1.55 ± 0.22	1.00 ± 0.07	0.70 ± 0.03	2.94 ± 0.28	1.51 ± 0.03	1.37 ± 0.05
σ_y [MPa]	6.04 ± 0.24	5.83 ± 0.39	3.83 ± 0.47	17.37 ± 0.2	10.64 ± 0.7	9.77 ± 0.8

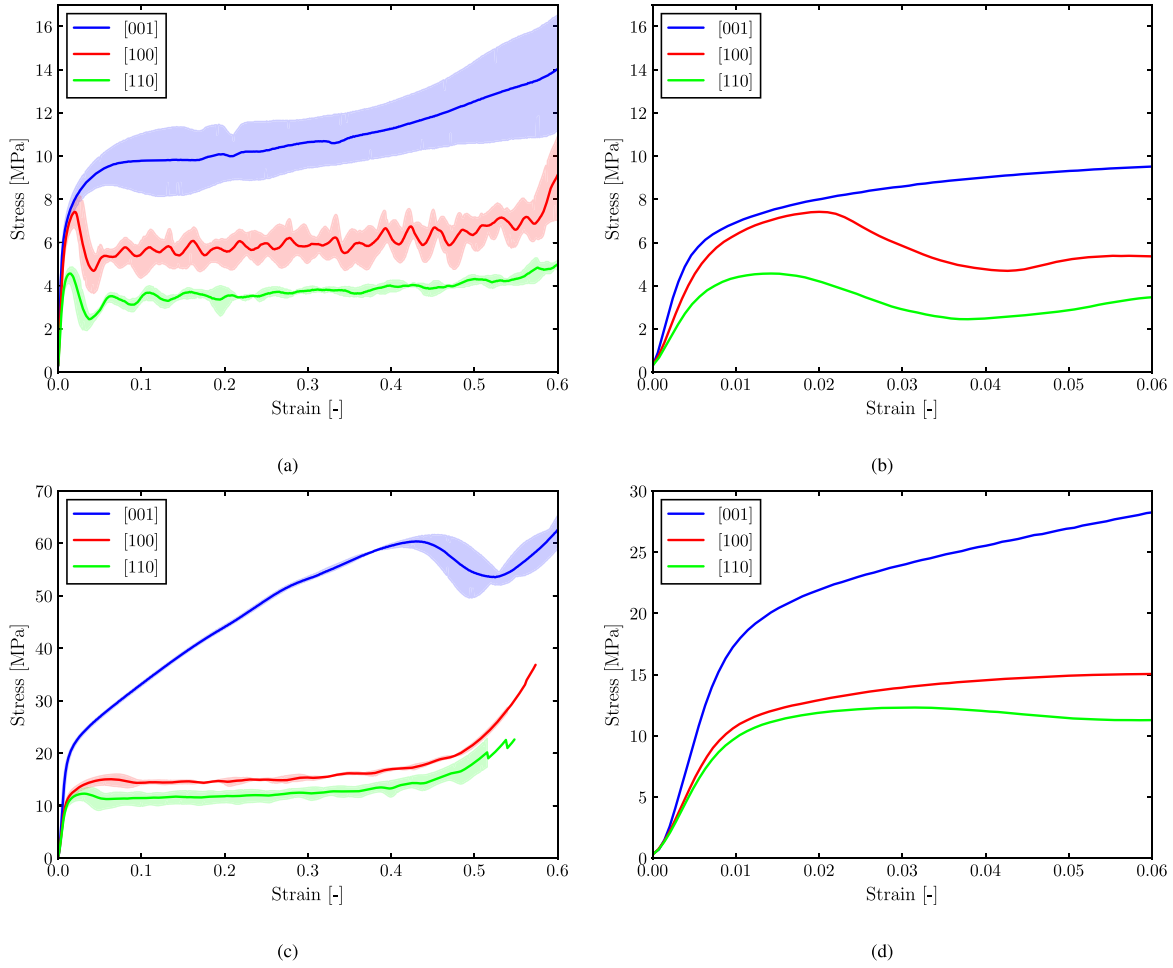

Fig. 15. Stress–strain curves of specimens under [001], [100] and [110] load directions for batch A (a) until densification and (b) until $\varepsilon = 0.06$; and batch B (c) until densification and (d) until $\varepsilon = 0.06$.

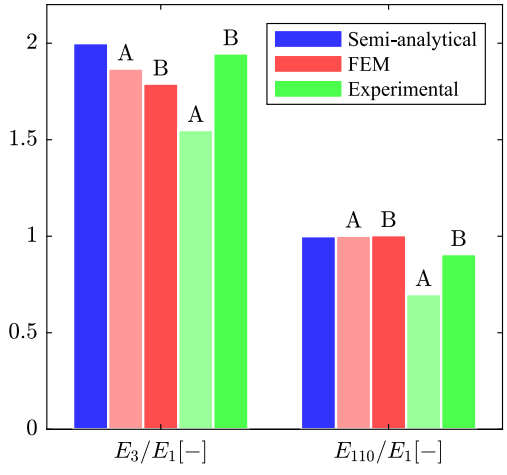

Fig. 16. Elastic moduli ratios for semi-analytical model and numerical and experimental values of structures A and B.

4. Discussion

4.1. Validity of semi-analytical model

In this work a semi-analytical model was developed to design transversely isotropic porous structures. The model shows good correlation with numerical results, even if the overall accuracy decreases for higher relative densities and E_3/E_1 ratios. This deviation can be attributed to the arise of bending loads and stress triaxialities as the slenderness of the struts decreases.

Experimental tests were also carried out with structures A and B, but the absolute mechanical properties are not compared directly to the values predicted by the semi-analytical and numerical models, since the manufacturing imperfections of the VFCCBCC unit cell cause an important decrease of stiffness and strength. These imperfections include strut waviness, dross formation, surface roughness, etc. These types of deviations are more common when manufacturing thin struts or small unit cell sizes and their detrimental effect on mechanical properties has been broadly studied [45–47]. Moreover, these imperfections may

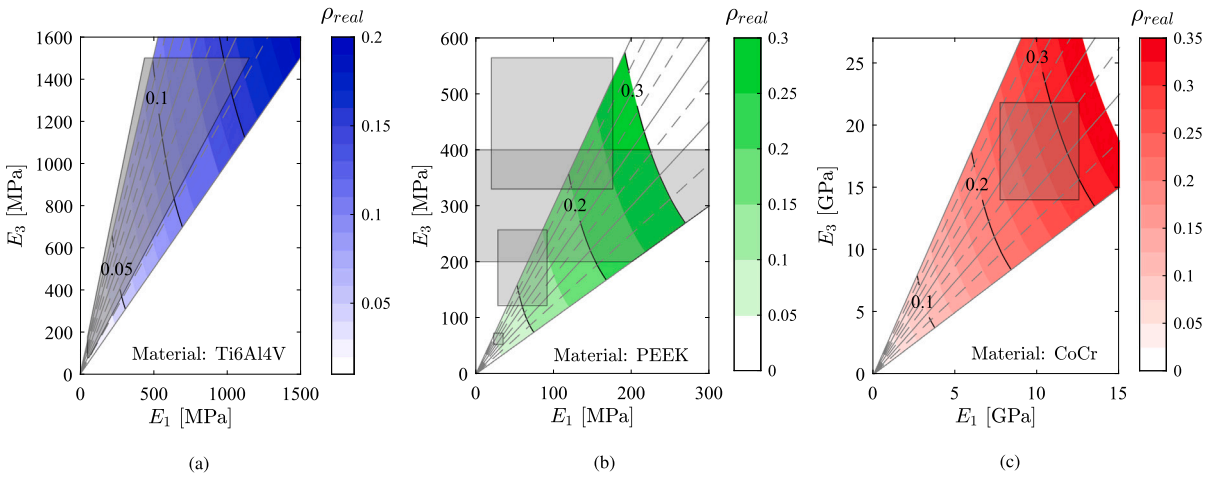

Fig. 17. Stiffness values in main and transverse orientations in implants for (a) proximal tibia [30], (b) spine [16,22,50,51], and (c) load bearing cortical bone [9].

change the anisotropy characteristics of the lattice structures [29,48], as can be observed by comparing the A and B structures.

The similarity of the experimental anisotropy levels of structure B with designed values compared to the structure A might be attributed to lower imperfection levels due to larger strut diameters for structure B. This indicates that the semi-analytical model can be used to design unit cells with prescribed anisotropy. Furthermore, the good agreement between analytical and numerical models suggests that reducing the level of imperfection e.g. increasing unit cell size, the absolute mechanical properties of the structures can be better predicted.

4.2. Patient-specific scaffold design

The developed semi-analytical model enables to design scaffolds that mimic various stiffness ratios that appear in bone tissue. Thus, patient-specific bone volume fraction and anisotropy can be used as input values to design implants with equivalent stiffness in different directions, reducing peri-implant stress and strain distortions. Furthermore, with the obtained model, different elastic moduli can be achieved in the principal direction for a prescribed porosity by varying the E_3/E_1 ratio, while for regular lattice structures each porosity value corresponds to a unique value of elastic modulus (Gibson–Ashby model [49]).

This feature can be used to implement the model in the biomedical sector, specifically for the design of patient-specific implants. To show the utility of this model for implant applications, three case studies are depicted in Fig. 17: (a) knee replacement in proximal tibia, (b) spine cancellous bone, and (c) load bearing cortical bone in different sites, such as femur. The colored surfaces represent the possible E_1 and E_3 values of the semi-analytical model for each value of relative density, while the gray areas correspond to the stiffness of bones in literature. A different parent material was chosen for each site to better match the target elastic properties, while also considering biocompatibility of the materials: Ti6Al4V for knee replacement, PEEK for spine cancellous bone, and CoCr for various cortical bones.

Knee replacements are in the increase due to the prevalence of osteoarthritis in the knee joint. The proximal tibia, which is replaced by this surgery, is mainly loaded in compression along the anatomical axis; thus, the design of knee implants should be based on bone elastic modulus in that direction (81 and 1500 MPa) with a degree of anisotropy ranging from 1.3 to 3.4 [21]. Fig. 17(a) shows the possible design space of the semi-analytical model to match the stiffness range of the proximal tibia in E_1 and E_3. The model covers a great part of the proximal tibia stiffness range, even if the manufacturing below relative densities of 0.1 can be challenging, and possibly larger unit cell sizes are required for such designs. It must be noted that a Young's modulus of 37.5 GPa was given to the Ti6Al4V parent material. This low modulus is a result of tensile tests of micro-struts to implicitly consider the manufacturing deviations of strut-based lattice structures [52].

The spine is also mainly loaded along its anatomical axis, and its cancellous bone can have a wide range of stiffness values according to different studies, with E_3/E_1 ratios as high as 7.3 [16,22,50,51]. In this case, PEEK (E = 4 GPa) was chosen as parent material to match the elastic behavior of the spine. The design space of the semi-analytical model covers most of the E_3 stiffness ranges within relative densities between 0.1 and 0.3, as depicted in Fig. 17(b). On the other hand, some of the E_3/E_1 ratios of the spine exceed the design space of the transversely isotropic model. In these cases it is possible to match the E_3 stiffness along the anatomical axis, at the cost of having a higher E_1 value in the transverse plane.

The cortical bone is transversely isotropic due to its microstructure, which is formed by aligned osteons that give superior stiffness along the diaphyseal axis, and inferior isotropic stiffness in the transverse plane [9,23,53]. For Fig. 17(c) CoCr (E = 200 GPa) was assigned as parent material to enhance the stiffness of the design space of the semi-analytical model and mimic the elastic behavior of cortical bone. Thus, the model perfectly covers the E_3 and E_1 values found in literature, even if in some cases high relative densities above 0.3 are required. On the other hand, these stiffness values are expected for perfectly manufactured structures, which is rarely the case in additively manufactured scaffolds. The unit cell size should be increased to have larger features to be manufactured with a reduced imperfection level to reach stiffness levels predicted by the model.

The transversely isotropic scaffolds aligned with the main load direction allow the design of lighter implants due to the reduced mass in the transverse direction. This also means that higher permeability can be achieved, enhancing bone ingrowth and vascularization within the implant while ensuring necessary stiffness and strength in the direction of the main load. This model could be implemented into optimization algorithms with other analytical models describing the permeability of the structure to design optimal and personalized implants based on the bone site and characteristics of the bone patient [32]. Moreover, the established relationship between the morphology of stretch dominated lattice structures and their orthotropic effective stiffness matrix enables optimization-based design to tailor the stiffness of different bone sites while also considering bone site specific anisotropy.

5. Conclusions

A semi-analytical model was developed to design transversely isotropic lattice structures with prescribed stiffness ratios between the longitudinal and transverse directions. Numerical and experimental

analyses were performed to test the validity of the designs, and the main conclusions are as follows:

- The developed semi-analytical model effectively describes a transversely isotropic elastic behavior, with ellipsoidal directional stiffness, which enables the design of unit cells with prescribed anisotropy.
- The obtained semi-analytical model is capable of mimicking the stiffness and anisotropy of different bone sites such as proximal tibia, spine or femoral cortical bone. By correctly aligning the scaffold with the principal directions of the bone, a higher porosity of the scaffolds can be achieved compared to other isotropic counterparts.
- Many possible strut configurations are available to obtain a prescribed transverse isotropy. This work analyzed the VFCCBCC unit cell in more detail, and SC2BCC and SC2FCC2 were also presented as viable for transverse isotropy.
- The elastic constants obtained from numerical models of VFCCBCC unit cell are in good agreement with the semi-analytical model. The accuracy of the model decreases with an increase of relative density, and higher E_3/E_1 ratios also have a detrimental effect.
- Quasi-static compressive tests indicate that prescribed anisotropy can be achieved with the VFCCBCC unit cell, even if for lower relative densities the deviations from designed parameters increase due to the manufacturing defects.

Declaration of competing interest

The authors declare that they have no known competing financial interests or personal relationships that could have appeared to influence the work reported in this paper.

Acknowledgment

This research did not receive any specific grant from funding agencies in the public, commercial, or not-for-profit sectors.

Appendix A. Supplementary data

Supplementary material related to this article can be found online at https://doi.org/10.1016/j.compbiomed.2022.105761.

References

[1] M. Leary, M. Mazur, J. Elambasseril, M. Mcmillan, T. Chirent, Y. Sun, M. Qian, M. Easton, M. Brandt, Selective laser melting (SLM) of AlSi12Mg lattice structures, Mater. Des. 98 (2016) 344–357, http://dx.doi.org/10.1016/j.matdes.2016.02.127.

[2] A. Azarniya, X.G. Colera, M.J. Mirzaali, S. Sovizi, F. Bartolomeu, M.k. St Weglowski, W.W. Wits, C.Y. Yap, J. Ahn, G. Miranda, F.S. Silva, H.R. Madaah Hosseini, S. Ramakrishna, A.A. Zadpoor, Additive manufacturing of Ti–6Al–4V parts through laser metal deposition (LMD): Process, microstructure, and mechanical properties, J. Alloys Compd. 804 (2019) 163–191, http://dx.doi.org/10.1016/J.JALLCOM.2019.04.255.

[3] I. Gibson, D. Rosen, B. Stucker, Powder bed fusion processes, in: Additive Manufacturing Technologies, Springer, 2015, pp. 107–145.

[4] A. M.F, The properties of foams and lattices, Phil. Trans. R. Soc. A 364 (1838) (2006) 15–30, http://dx.doi.org/10.1098/rsta.2005.1678.

[5] V.S. Deshpande, M.F. Ashby, N.A. Fleck, Foam topology: Bending versus stretching dominated architectures, Acta Mater. 49 (2001) 1035–1040, http://dx.doi.org/10.1016/S1359-6454(00)00379-7.

[6] T. Maconachie, M. Leary, B. Lozanovski, X. Zhang, M. Qian, O. Faruque, M. Brandt, SLM lattice structures: Properties, performance, applications and challenges, Mater. Des. 183 (2019) 108137, http://dx.doi.org/10.1016/j.matdes.2019.108137.

[7] H. Chen, Y. Liu, C. Wang, A. Zhang, B. Chen, Q. Han, J. Wang, Design and properties of biomimetic irregular scaffolds for bone tissue engineering, Comput. Biol. Med. 130 (2021) 104241, http://dx.doi.org/10.1016/J.COMPBIOMED.2021.104241.

[8] E. Davoodi, H. Montazerian, A.S. Mirhakimi, M. Zhianmanesh, O. Ibhadode, S.I. Shahabad, R. Esmaeilizadeh, E. Sarikhani, S. Toorandaz, S.A. Sarabi, R. Nasiri, Y. Zhu, J. Kadkhodapour, B. Li, A. Khademhosseini, E. Toyserkani, Additively manufactured metallic biomaterials, Bioact. Mater. 15 (2022) 214–249, http://dx.doi.org/10.1016/J.BIOACTMAT.2021.12.027.

[9] X. Wang, S. Xu, S. Zhou, W. Xu, M. Leary, P. Choong, M. Qian, M. Brandt, Y.M. Xie, Topological design and additive manufacturing of porous metals for bone scaffolds and orthopaedic implants: A review, Biomaterials 83 (2016) 127–141.

[10] R.S. Abass, M. Al Ali, M. Al Ali, Shape and topology optimization design for total hip joint implant, in: Proceedings of the World Congress on Engineering 2019, London, U.K., 2019.

[11] A.A. Zadpoor, Mechanical performance of additively manufactured meta-biomaterials, Acta Biomater. 85 (2019) 41–59, http://dx.doi.org/10.1016/J.ACTBIO.2018.12.038.

[12] S. Ghouse, N. Reznikov, O.R. Boughton, S. Babu, K.C. Ng, G. Blunn, J.P. Cobb, M.M. Stevens, J.R. Jeffers, The design and in vivo testing of a locally stiffness-matched porous scaffold, Appl. Mater. Today 15 (2019) 377–388, http://dx.doi.org/10.1016/J.APMT.2019.02.017.

[13] S. Li, E. Demirci, V.V. Silberschmidt, Variability and anisotropy of mechanical behavior of cortical bone in tension and compression, J. Mech. Behav. Biomed. Mater. 21 (2013) 109–120, http://dx.doi.org/10.1016/J.JMBBM.2013.02.021.

[14] Z. Tabor, E. Rokita, Quantifying anisotropy of trabecular bone from gray-level images, Bone 40 (4) (2007) 966–972, http://dx.doi.org/10.1016/J.BONE.2006.10.022.

[15] G. Maquer, S.N. Musy, J. Wandel, T. Gross, P.K. Zysset, Bone volume fraction and fabric anisotropy are better determinants of trabecular bone stiffness than other morphological variables, J. Bone Miner. Res. 30 (6) (2015) 1000–1008, http://dx.doi.org/10.1002/JBMR.2437.

[16] P. Augat, T. Link, T.F. Lang, J.C. Lin, S. Majumdar, H.K. Genant, Anisotropy of the elastic modulus of trabecular bone specimens from different anatomical locations, Med. Eng. Phys. 20 (2) (1998) 124–131, http://dx.doi.org/10.1016/S1350-4533(98)00001-0.

[17] S.H. Liao, R.F. Tong, J.X. Dong, Influence of anisotropy on peri-implant stress and strain in complete mandible model from CT, Comput. Med. Imaging Graph. 32 (1) (2008) 53–60, http://dx.doi.org/10.1016/J.COMPMEDIMAG.2007.09.001.

[18] Z. Gümrükçü, Y.T. Korkmaz, F.M. Korkmaz, Biomechanical evaluation of implant-supported prosthesis with various tilting implant angles and bone types in atrophic maxilla: A finite element study, Comput. Biol. Med. 86 (2017) 47–54, http://dx.doi.org/10.1016/J.COMPBIOMED.2017.04.015.

[19] V.-H. Nguyen, G. Rosi, S. Naili, A. Michel, M.-L. Raffa, R. Bosc, J.-P. Meningaud, C. Chappard, N. Takano, G. Haiat, Influence of anisotropic bone properties on the biomechanical behavior of the acetabular cup implant: a multiscale finite element study, Comput. Methods Biomech. Biomed. Eng. 20 (12) (2017) 1312–1325.

[20] J. Kang, E. Dong, D. Li, S. Dong, C. Zhang, L. Wang, Anisotropy characteristics of microstructures for bone substitutes and porous implants with application of additive manufacturing in orthopaedic, Mater. Des. 191 (2020) 108608, http://dx.doi.org/10.1016/j.matdes.2020.108608.

[21] M. Munford, U. Hossain, S. Ghouse, J.R. Jeffers, Prediction of anisotropic mechanical properties for lattice structures, Addit. Manuf. 32 (2020) 101041, http://dx.doi.org/10.1016/j.addma.2020.101041.

[22] A.K. Aiyangar, J. Vivanco, A.G. Au, P.A. Anderson, E.L. Smith, H.-L. Ploeg, Dependence of anisotropy of human lumbar vertebral trabecular bone on quantitative computed tomography-based apparent density, J. Biomech. Eng. 136 (9) (2014).

[23] S. Bernard, Q. Grimal, P. Laugier, Accurate measurement of cortical bone elasticity tensor with resonant ultrasound spectroscopy, J. Mech. Behav. Biomed. Mater. 18 (2013) 12–19, https://doi.org/10.1016/j.jmbbm.2012.09.017.

[24] M.C. Messner, M.I. Barham, M. Kumar, N.R. Barton, Wave propagation in equivalent continuums representing truss lattice materials, Int. J. Solids Struct. 73 (2015) 55–66.

[25] T. Tancogne-Dejean, D. Mohr, Elastically-isotropic truss lattice materials of reduced plastic anisotropy, Int. J. Solids Struct. 138 (2018) 24–39.

[26] R.M. Latture, M.R. Begley, F.W. Zok, Design and mechanical properties of elastically isotropic trusses, J. Mater. Res. 33 (3) (2018) 249–263.

[27] V.J. Challis, X. Xu, L.C. Zhang, A.P. Roberts, J.F. Grotowski, T.B. Sercombe, High specific strength and stiffness structures produced using selective laser melting, Mater. Des. 63 (2014) 783–788, http://dx.doi.org/10.1016/j.matdes.2014.05.064.

[28] S. Xu, J. Shen, S. Zhou, X. Huang, Y.M. Xie, Design of lattice structures with controlled anisotropy, Mater. Des. 93 (2016) 443–447, http://dx.doi.org/10.1016/j.matdes.2016.01.007.

[29] A. Cutolo, B. Engelen, W. Desmet, B. Van Hooreweder, Mechanical properties of diamond lattice Ti–6Al–4V structures produced by laser powder bed fusion: On the effect of the load direction, J. Mech. Behav. Biomed. Mater. 104 (2020) 103656, http://dx.doi.org/10.1016/j.jmbbm.2020.103656.

[30] M. Munford, U. Hossain, S. Ghouse, J.R. Jeffers, Prediction of anisotropic mechanical properties for lattice structures, Addit. Manuf. 32 (2020) 101041.

[31] U. Hossain, S. Ghouse, K. Nai, J.R. Jeffers, Controlling and testing anisotropy in additively manufactured stochastic structures, Addit. Manuf. 39 (2021) 101849.
[32] R. Asbai-Ghoudan, S. Ruiz de Galarreta, N. Rodriguez-Florez, Analytical model for the prediction of permeability of triply periodic minimal surfaces, J. Mech. Behav. Biomed. Mater. 124 (2021) 104804, http://dx.doi.org/10.1016/J.JMBBM.2021.104804.
[33] M. Alaña, A. Lopez-Arancibia, A. Pradera-Mallabiabarrena, S. Ruiz de Galarreta, Analytical model of the elastic behavior of a modified face-centered cubic lattice structure, J. Mech. Behav. Biomed. Mater. 98 (2019) http://dx.doi.org/10.1016/j.jmbbm.2019.05.043.
[34] M. Zhang, Z. Yang, Z. Lu, B. Liao, X. He, Effective elastic properties and initial yield surfaces of two 3D lattice structures, Int. J. Mech. Sci. 138–139 (2018) 146–158, http://dx.doi.org/10.1016/J.IJMECSCI.2018.02.008.
[35] A.A. Espinoza Orías, J.M. Deuerling, M.D. Landrigan, J.E. Renaud, R.K. Roeder, Anatomic variation in the elastic anisotropy of cortical bone tissue in the human femur, J. Mech. Behav. Biomed. Mater. 2 (3) (2009) 255–263, http://dx.doi.org/10.1016/J.JMBBM.2008.08.005.
[36] S.W. Shore, P.E. Barbone, A.A. Oberai, E.F. Morgan, Transversely isotropic elasticity imaging of cancellous bone, J. Biomech. Eng. 133 (6) (2011) http://dx.doi.org/10.1115/1.4004231.
[37] R.G. Hutchinson, N.A. Fleck, The structural performance of the periodic truss, J. Mech. Phys. Solids 54 (4) (2006) 756–782.
[38] V. Karageorgiou, D. Kaplan, Porosity of 3D biomaterial scaffolds and osteogenesis, Biomaterials 26 (27) (2005) 5474–5491, http://dx.doi.org/10.1016/j.biomaterials.2005.02.002.
[39] C. Metz, G.N. Duda, S. Checa, Towards multi-dynamic mechano-biological optimization of 3D-printed scaffolds to foster bone regeneration, Acta Biomater. 101 (2020) 117–127, http://dx.doi.org/10.1016/J.ACTBIO.2019.10.029.
[40] C. Elangeswaran, A. Cutolo, G.K. Muralidharan, C. de Formanoir, F. Berto, K. Vanmeensel, B. Van Hooreweder, Effect of post-treatments on the fatigue behaviour of 316L stainless steel manufactured by laser powder bed fusion, Int. J. Fatigue 123 (2019) 31–39, http://dx.doi.org/10.1016/j.ijfatigue.2019.01.013.
[41] S.L. Omairey, P.D. Dunning, S. Sriramula, Development of an ABAQUS plugin tool for periodic RVE homogenisation, Eng. Comput. 35 (2) (2018) 567–577, http://dx.doi.org/10.1007/s00366-018-0616-4.
[42] S. Ruiz de Galarreta, J.R. Jeffers, S. Ghouse, A validated finite element analysis procedure for porous structures, Mater. Des. 189 (2020) 108546, http://dx.doi.org/10.1016/j.matdes.2020.108546.
[43] X. Yan, Q. Li, S. Yin, Z. Chen, R. Jenkins, C. Chen, J. Wang, W. Ma, R. Bolot, R. Lupoi, Z. Ren, H. Liao, M. Liu, Mechanical and in vitro study of an isotropic Ti6Al4V lattice structure fabricated using selective laser melting, J. Alloys Compd. 782 (2019) 209–223, http://dx.doi.org/10.1016/J.JALLCOM.2018.12.220.
[44] ISO 13314:2011 - Mechanical testing of metals – Ductility testing – Compression test for porous and cellular metals, 2011.
[45] D. Melancon, Z. Bagheri, R. Johnston, L. Liu, M. Tanzer, D. Pasini, Mechanical characterization of structurally porous biomaterials built via additive manufacturing: experiments, predictive models, and design maps for load-bearing bone replacement implants, Acta Biomater. 63 (2017) 350–368, http://dx.doi.org/10.1016/j.actbio.2017.09.013.
[46] D. Mahmoud, K.S. Al-Rubaie, M.A. Elbestawi, The influence of selective laser melting defects on the fatigue properties of Ti6Al4V porosity graded gyroids for bone implants, Int. J. Mech. Sci. 193 (2021) 106180, http://dx.doi.org/10.1016/j.ijmecsci.2020.106180.
[47] L. Xiao, S. Li, W. Song, X. Xu, S. Gao, Process-induced geometric defect sensitivity of Ti–6Al–4V lattice structures with different mesoscopic topologies fabricated by electron beam melting, Mater. Sci. Eng. A 778 (2020) 139092, http://dx.doi.org/10.1016/j.msea.2020.139092.
[48] M. Alaña, A. Cutolo, G. Probst, S. Ruiz de Galarreta, B. Van Hooreweder, Understanding elastic anisotropy in diamond based lattice structures produced by laser powder bed fusion: Effect of manufacturing deviations, Mater. Des. 195 (2020) 108971, http://dx.doi.org/10.1016/j.matdes.2020.108971.
[49] M.F. Ashby, L.J. Gibson, Cellular Solids: Structure and Properties, Press Syndicate of the University of Cambridge, Cambridge, UK, 1997, pp. 175–231.
[50] A.M. Arefin, M. Lahowetz, P.F. Egan, Simulated tissue growth in tetragonal lattices with mechanical stiffness tuned for bone tissue engineering, Comput. Biol. Med. 138 (2021) 104913, http://dx.doi.org/10.1016/J.COMPBIOMED.2021.104913.
[51] S. Dendorfer, H.J. Maier, D. Taylor, J. Hammer, Anisotropy of the fatigue behaviour of cancellous bone, J. Biomech. 41 (3) (2008) 636–641.
[52] U. Hossain, S. Ghouse, K. Nai, J.R. Jeffers, Mechanical and morphological properties of additively manufactured SS316L and Ti6Al4V micro-struts as a function of build angle, Addit. Manuf. 46 (2021) 102050, http://dx.doi.org/10.1016/J.ADDMA.2021.102050.
[53] I. Sevostianov, M. Kachanov, Impact of the porous microstructure on the overall elastic properties of the osteonal cortical bone, J. Biomech. 33 (7) (2000) 881–888.